Modeling of ferrite formation in a duplex stainless steel weld considering non-uniform starting microstructure

W. Zhang [a], T. DebRoy [a,*], T.A. Palmer [b], J.W. Elmer [b]

[a] *Department of Materials Science and Engineering, The Pennsylvania State University, 115 Steidle Building, University Park, PA 16802, USA*
[b] *Lawrence Livermore National Laboratory, Livermore, CA 94551, USA*

Abstract

A one-dimensional numerical diffusion model has been developed to simulate the kinetics of the austenite (γ) to ferrite (δ) transformation in 2205 duplex stainless steel during welding. In this model, it is assumed that the transformation is driven by the diffusion of nitrogen under para-equilibrium conditions. Transformation kinetics from both uniform and non-uniform starting microstructures are investigated. The uniform starting structure is accounted for by using a pair of γ and δ grains of constant sizes, whereas non-uniform structures are simulated by considering four γ and δ grains of varying sizes. Interactions between neighboring grains, particularly hard and soft impingements, are taken into account by properly adjusting the boundary conditions. It is found that the transformation may take 30% more time for the non-uniform starting microstructure, where the ratio of thickest to thinnest grains is about 2, than for the uniform structure under typical weld heating conditions. Time–temperature-transformation and continuous-heating-transformation diagrams are constructed using the numerical diffusion model, providing a graphical means for predicting the kinetics of the $\gamma \rightarrow \delta$ transformation. The computed results were confirmed by experiments using an in-situ X-ray diffraction technique, thus validating the model.
© 2005 Acta Materialia Inc. Published by Elsevier Ltd. All rights reserved.

Keywords: Phase transformation; Duplex stainless steel; Diffusion; Welding; Ferrite; Austenite; Modeling; Uniform and non-uniform microstructures

1. Introduction

Duplex stainless steels (DSS) are two-phase alloys consisting of approximately equal proportions of ferrite (δ) and austenite (γ) phases. This balanced microstructure offers a combination of high toughness, good weldability, satisfactory corrosion resistance, and high strength. The combination of these desirable properties cannot be easily achieved by either austenitic or ferritic stainless steels [1,2]. Significant degradation of properties occurs if the balanced microstructure of the base metal is appreciably altered. The performance of DSS can

be significantly affected by welding-induced phase transformations, and understanding of the evolution of microstructure during welding is needed in order to predict the final weld properties.

During fusion welding, the DSS base metal is subjected to spatially and temporally non-uniform heating and cooling conditions. As a result, a series of complex microstructural transformations occur during welding, altering the δ/γ phase balance in the base metal. In the weld heat-affected zone (HAZ), for example, the microstructure undergoes both rapid heating and cooling cycles which vary depending on location and drive the δ/γ transformations to different levels of completion. In order to understand and predict the final microstructure in the HAZ, the kinetics of the $\gamma \rightarrow \delta$ transformation

---

* Corresponding author.
  E-mail address: debroy@psu.edu (T. DebRoy).

during the weld heating cycles must first be investigated so that the grain size, phase fraction, and concentration homogeneity of the transformed δ phase can be understood [1–3].

Several researchers have analyzed the δ/γ transformations in the HAZ of a 2205 DSS using the thermodynamics and kinetics of phase transformations [3–5]. Hertzman et al. [5] applied a model based upon Cahn's theory of grain boundary nucleated reactions to calculate the kinetics of the δ → γ transformation during cooling. The growth rate of the precipitates was calculated using the analytical solution of diffusion-controlled particle growth proposed by Engberg et al. [6] for both spherical and planar geometries. Hemmer et al. [3,4] investigated the kinetics of the γ → δ transformation during heating and proposed an analytical model based on nitrogen diffusion and considering the effect of soft impingement. Their model assumes that nitrogen diffuses only in the δ phase and that the resulting nitrogen concentration profile in the δ phase is linear [4]. Although these analytical models have been useful in understanding the phase transformation kinetics, the accuracy of the calculations was limited by several simplifying assumptions.

In this study, a numerical model was developed to calculate the γ → δ transformation kinetics under heating rates typical of welding. This model removes some of the simplifying assumptions of the previous analytical models and addresses more realistic situations. It is assumed that the rate of the γ → δ transformation during heating is controlled by nitrogen diffusion in both the γ and δ phases. Local equilibrium of nitrogen is assumed to be maintained at the δ/γ interface, and the partitioning of substitutional elements is ignored. Furthermore, unlike conventional diffusion models that assume a uniform starting microstructure [7–10], the model presented here considers the effect of non-uniform starting microstructure on the transformation kinetics, thus allowing the effects of existing grain boundaries (hard impingement) and overlapping diffusion fields (soft impingement) on transformation kinetics to be studied.

In order to calculate the kinetics of the diffusion controlled transformation, the thermal cycles in the weld must be known. Since experimental measurements of such data are difficult, a well-tested thermo-fluid model [11,12] was used to calculate the thermal cycles of the weld. Using the numerical diffusion model and computed heating rates, the kinetics of the γ → δ transformation at various locations in the HAZ of a 2205 DSS weld could be calculated. Time–temperature-transformation (TTT) and continuous-heating-transformation (CHT) diagrams for the 2205 DSS were constructed using the diffusion model and validated by comparing the calculated results with data obtained using a spatially resolved X-ray diffraction (SRXRD) technique [13–19]. Combination of the numerical diffusion model,

weld thermo-fluid simulation, and SRXRD experiments provided useful insights into the mechanism and kinetics of the γ → δ transformation during welding of duplex stainless steels.

2. Mathematical modeling

Two numerical models were used in the present study: a numerical diffusion model and a weld thermo-fluid model. This latter model was used to compute the temperature versus time data in the weldment. These computed thermal cycles were then used in the numerical diffusion model to determine the rates of the γ → δ transformation during weld heating.

2.1. Diffusion model considering non-uniform starting microstructure

2.1.1. Representation of starting microstructure

Fig. 1 shows the base metal microstructure of the 2205 DSS used in this study. It consists of alternate layers of δ-ferrite and γ-austenite phases in nearly equal amounts (54% of δ and 46% of γ). In order to achieve this starting microstructure, the material has been solution annealed at a temperature of 1338 K for a period of 2.5 h, followed by water quenching to ambient temperatures. Therefore, the starting microstructure is metastable and non-homogeneous. Since no significant transformation was observed below the solution annealing temperature [18,19], this base metal microstructure is assumed to represent the microstructure at the initiation of the γ → δ transformation at elevated temperatures. The initial thicknesses, phase fractions and nitrogen concentrations of the δ and γ plates in the base metal were measured and are summarized in Table 1 [18,19].

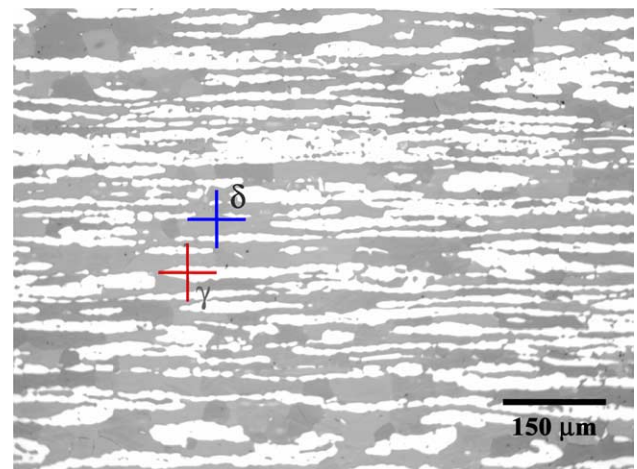Fig. 1. Optical microstructure of the base metal of the 2205 DSS [18,19]. The γ-austenite appears light and the δ-ferrite appears dark. The chemical composition is the following (by wt.%): 22.43 Cr, 4.88 Ni, 3.13 Mo, 1.40 Mn, 0.18 N, 0.023 C, 0.004 S, 0.67 Si and balance Fe.

Table 1
Experimentally measured microstructure of the 2205 DSS base metal [19]

Phase	Average grain thickness (µm)	Phase fraction	Nitrogen concentration (wt.%)
δ-Ferrite	22.3	0.54	0.03
γ-Austenite	19.0	0.46	0.356

Much of the previous research on diffusion-controlled phase transformations considers uniform initial grain sizes equal to average grain sizes of the material [7–10]. In order to provide a baseline for comparing the present modeling results with previous studies, a system with uniform grain sizes is first considered. Fig. 2(a) depicts the calculation domain consisting of half of a γ grain and half of a δ grain with symmetric boundary conditions at both ends. Such a system implies a uniform starting microstructure, where the γ and δ grains have constant sizes specific to the phase. Although previous analyses of uniform structures have provided much useful insight into transformation kinetics, a uniform starting microstructure rarely occurs in engineering materials, where a measurable distribution of grain sizes exists about the mean value. One goal of this investigation was to determine whether the non-uniformity of the starting microstructure affects the phase transformation rates.

In the present study, the calculation domain shown in Fig. 2(b) is used to represent the non-uniform starting microstructure. This structure consists of two types of γ grains of distinct sizes (γ₁ and γ₂) as well as two types of δ grains of different sizes (δ₁ and δ₂). Fig. 2(b) shows that the selected computational domain is an exact mirror of its neighbors due to the symmetric boundary conditions applied at both ends of the domain. In the calculation domain shown in Fig. 2(b), there are one

and a half γ grains (one $\gamma_1 + 1/2\gamma_2$) and one and a half δ grains ($1/2\delta_1$ + one δ_2). In other words, the number of γ_2 grains is twice that of γ_1 grains, and the same proportion is true for the numbers of δ_2 and δ_1 grains. It is important to note that a planar geometry is considered in the one-dimensional diffusion model. Therefore, the interfacial area between the δ and γ phases is independent of the thickness of either phase, and depends on only the numbers of the phase boundaries. For all of the simulated microstructures, the calculation domain initially has three phase boundaries, and the initial interfacial area is therefore held constant. Varying the initial interfacial area between the two phases, by increasing or decreasing the number of grains within the calculation domain, would yield different results.

In the subsequent discussion, for the clarity and simplicity of the presentation, the diffusion problem is first solved for the uniform microstructure shown in Fig. 2(a). The phase transformation rates for differing degrees of microstructural non-uniformity are then calculated using the diffusion domain shown in Fig. 2(b).

2.1.2. Governing equations of nitrogen diffusion

Under the rapid heating conditions encountered during welding, the $\gamma \rightarrow \delta$ phase transformation is assumed to be controlled by the para-equilibrium diffusion of nitrogen [3–5]. This approximation is reasonable, given that the available time for the transformation is short and the substitutional elements cannot redistribute within the two phases because of insufficient time. Since the as-received 2205 DSS was solution treated at an elevated temperature, it is assumed that the nitrogen, a strong austenite stabilizer, is distributed evenly in each phase in the starting microstructure, with the γ phase being richer in nitrogen than the δ phase. Fig. 3(a) shows a schematic concentration profile of nitrogen along the X direction in the base plate, where $N_{\delta,0}$ and $N_{\gamma,0}$ represent the initial concentrations of nitrogen in the δ and γ phases, respectively. Local equilibrium of nitrogen is
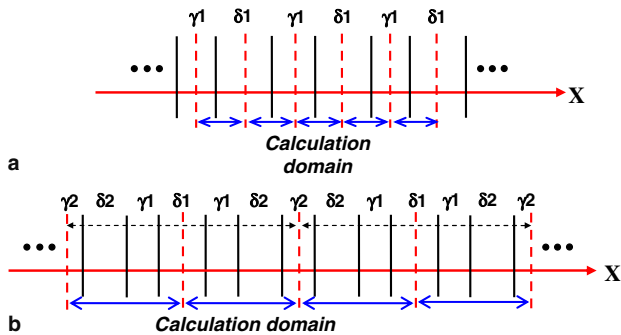

Fig. 2. Schematic plot showing the calculation domains used to represent different starting microstructures: (a) uniform structure, and (b) non-uniform structure with two different γ and δ grain sizes. Solid lines are the δ/γ grain boundaries, while dashed vertical lines are the δ and γ grain centers where symmetric boundary conditions are applied. The dashed horizontal arrows represent the repeating cells of the starting microstructure.
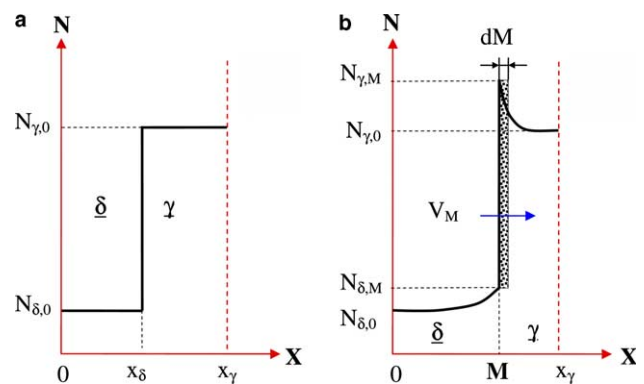

Fig. 3. Schematic plot showing (a) the initial nitrogen concentration profile, and (b) the nitrogen concentration profile during the transformation.

assumed at the δ/γ interface, and the partitioning of the other alloying elements is assumed to be negligible during the $\gamma \rightarrow \delta$ transformation.

Fig. 3(b) shows the nitrogen concentration profile during the $\gamma \rightarrow \delta$ transformation, where M is the δ/γ interface location, and $N_{\delta,M}$ and $N_{\gamma,M}$ are the concentrations of nitrogen at the δ/γ interface in the δ and γ phases, respectively. The nitrogen concentration as a function of time (t) and distance (x) is given by Fick's second law of diffusion [20]:

$$\frac{\partial N}{\partial t} = D_\delta \frac{\partial^2 N}{\partial x^2}, \quad \text{in } \delta \ (0 < x < M),$$
$$\frac{\partial N}{\partial t} = D_\gamma \frac{\partial^2 N}{\partial x^2}, \quad \text{in } \gamma \ (M < x < x_\gamma), \tag{1}$$

where N is the nitrogen concentration, t is time, and D_δ and D_γ are the diffusion coefficients of nitrogen in the δ and γ phases, respectively. The values for D_δ and D_γ are taken from existing literature and, for simplicity, are assumed to be independent of the alloy concentrations in both the δ and γ phases [3–7,21]. The diffusion coefficient of nitrogen in the δ phase of the 2205 DSS as a function of temperature is given as [5]:

$$D_\delta = 0.464 \exp(-10223.7/T) \quad (\text{mm}^2 \text{ s}^{-1}). \tag{2}$$

The diffusion coefficient of nitrogen in γ for the 2205 DSS is not readily available in the literature, and is approximated by the diffusion coefficient of nitrogen in the pure γ-Fe [21].

$$D_\gamma = 36.0 \exp(-18883.8/T) \quad (\text{mm}^2 \text{ s}^{-1}). \tag{3}$$

The initial conditions for the concentration profile shown in Fig. 3(a) at a time equal to zero are given as

$$N = N_{\delta,0} \quad 0 \leqslant x \leqslant M,$$
$$N = N_{\gamma,0} \quad M \leqslant x \leqslant x_\gamma, \tag{4}$$
$$M = x_\delta.$$

The boundary conditions for the concentration profile shown in Fig. 3(b) at times greater than zero are given as

$$\frac{\partial N}{\partial x} = 0 \quad x = 0 \quad \text{and} \quad x = x_\gamma,$$
$$N = N_{\delta,M} \quad x = M^-, \tag{5}$$
$$N = N_{\gamma,M} \quad x = M^+,$$

where M^- and M^+ are the locations in δ and γ phases at the δ/γ interface, respectively. Eq. (5) indicates that there is no mass flux of nitrogen across the two boundary surfaces at $x = 0$ and x_γ and that the nitrogen concentrations in the δ and γ phases are in local equilibrium at the δ/γ interface.

Since the δ/γ interface moves during the transformation, its location (M) needs to be determined in order to solve Eq. (1). As shown in Fig. 3(b), in order for the interface to advance a distance of dM in a short time

period of dt, an equivalent amount of nitrogen needs to be diffused away. Therefore, the interface location as a function of time is given as

$$(N_{\gamma,M} - N_{\delta,M})\text{d}M = \left(D_\delta \frac{\partial N}{\partial x}\bigg|_{M^-} - D_\gamma \frac{\partial N}{\partial x}\bigg|_{M^+} \right)\text{d}t,$$
$$\text{or,} \ (N_{\gamma,M} - N_{\delta,M})\frac{\text{d}M}{\text{d}t} = D_\delta \frac{\partial N}{\partial x}\bigg|_{M^-} - D_\gamma \frac{\partial N}{\partial x}\bigg|_{M^+}, \tag{6}$$

where $\frac{\text{d}M}{\text{d}t}$ is the interface moving velocity (V_M), $(N_{\gamma,M} - N_{\delta,M})\text{d}M$ represents the nitrogen content in the shadowed area, and $D_\delta \frac{\partial N}{\partial x}\big|_{M^-}$ and $-D_\gamma \frac{\partial N}{\partial x}\big|_{M^+}$ are the nitrogen fluxes into the δ and γ phases, respectively. Eq. (6) indicates that the total mass of nitrogen in the system is conserved. As the thin γ layer with thickness of dM is dissolved, the nitrogen mass in this layer diffuses into the bulk regions of δ and γ. As a result, the nitrogen concentrations at the two symmetric boundaries, i.e., $x = 0$ and $x = x_\gamma$, increase, and the extent to which the concentration can rise is determined by the equilibrium nitrogen concentrations at the δ/γ phase interfaces. The nitrogen concentration profiles in δ and γ along with the fractions of these two phases are obtained by solving Eqs. (1) and (6) numerically to determine the interface location, as discussed in the following section.

2.1.3. Numerical solution

A widely-used numerical method developed by Murray and Landis for solving diffusion problems with moving interfaces [22,23] is employed to solve Eqs. (1) and (6). As shown in Fig. 4, the solution domain from $x = 0$ to $x = x_\gamma$ is discretized into n grid points at a time, t. The δ/γ interface, M, lies on a particular grid point (m), which moves with the interface, as shown in Fig. 4. If the interface advances to a new location at time $t + \Delta t$, all the interior grids proportionally move to the right so that the interface remains at grid point m. As a result, the spatial intervals of the grids vary with time. For this moving grid system, Eq. (1) is transformed into the following form [22,23]:
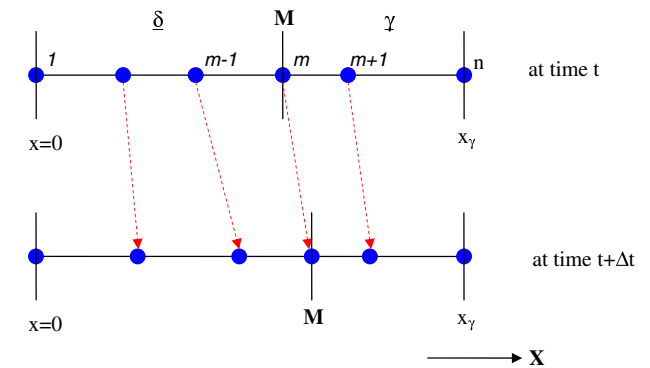

Fig. 4. Schematic representation of grids used in the numerical solution at time t and $t + \Delta t$.

$$\left.\frac{\partial N}{\partial t}\right|_i = D_\delta \frac{\partial^2 N}{\partial x^2} + \frac{x_i}{M} V_M \frac{\partial N}{\partial x} \quad \text{in } \delta \ (0 < x < M),$$

$$\left.\frac{\partial N}{\partial t}\right|_j = D_\gamma \frac{\partial^2 N}{\partial x^2} + \frac{x_j}{M} V_M \frac{\partial N}{\partial x} \quad \text{in } \gamma \ (M < x < x_\gamma),$$

(7)

where x_i and x_j are the locations of the ith and jth grid points, respectively, and $\frac{\partial N}{\partial t}|_i$ and $\frac{\partial N}{\partial t}|_j$ represent the change of nitrogen concentration with time at these same grid points. Comparing this equation with Eq. (1), the right most terms in Eq. (7) are used to account for the spatial movements of the grid nodes.

Eq. (7) is discretized using the control volume method with a fully-implicit scheme [24]. The general discretized equation at grid i is given as

$$a_P N_i = a_W N_{i-1} + a_E N_{i+1} + a_P^0 N_i^0 + Sc_i,$$

(8)

where N_i^0 is the nitrogen concentration at time t and all other concentrations are evaluated at time $t + \Delta t$ (fully-implicit). Symbols a_P, a_W, a_E, a_P^0 and Sc_i are coefficients formulated using the control volume method [24].

The interface moving velocity is discretized as

$$(N_{\gamma,M} - N_{\delta,M})V_M = D_\delta \frac{N_m - N_{m-1}}{x_m - x_{m-1}} - D_\gamma \frac{N_{m+1} - N_m}{x_{m+1} - x_m},$$

(9)

where m is the particular grid point where the interface is attached, and all the concentrations are evaluated at time $t + \Delta t$.

Once the interface moving velocity is obtained, the spatial locations of the grids (x_i) at time $t + \Delta t$ are updated using the following equation:

$$x_i = x_i^0 + \frac{x_i^0}{M^0} V_M \Delta t,$$

(10)

where Δt is the time step, and x_i^0 and M^0 are the locations of the ith grid point and interface at time t, respectively.

2.1.4. Non-uniform starting microstructure

In the preceding discussion, the governing equations of the $\gamma \to \delta$ transformation are formulated assuming a uniform starting grain structure. In this section, the numerical diffusion model is extended to non-uniform grain structures. For simplicity, the calculation domain consisting of two types of δ grains and two types of γ grains with varying thicknesses (Fig. 2(b)) was used to represent the starting microstructure. Although this system is simple, it allows the interactions between neighboring grains and the effects of soft and hard impingements to be examined.

Fig. 5 shows the initial nitrogen concentration profile in the calculation domain representing a non-uniform starting microstructure. This domain consists of a half of δ_1, one γ_1, one δ_2, and a half of γ_2, and symmetric conditions are applied at both ends of the domain. Three interface locations, i.e., M1, M2, and M3, are cal-
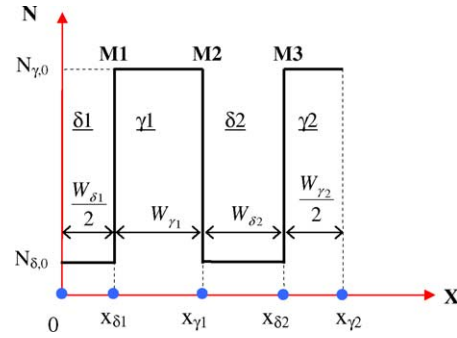

Fig. 5. The initial nitrogen concentration profile in the calculation domain with the non-uniform starting microstructure.

culated explicitly based on the nitrogen conservation at the interfaces. The extension of the governing equations (1) and (6) to the calculation domain shown in Fig. 5 is straightforward, and is therefore not described here.

Using this procedure, the interaction between neighboring grains can be examined. For instance, when a γ grain completely dissolves, the two neighboring δ grains may impinge on each other. Depending on the sizes of the γ grains, there are two possible circumstances of the γ dissolution. If γ_1 is smaller than γ_2, γ_1 will dissolve completely before γ_2 and vice versa. Under these conditions, the larger the size of a γ grain, the longer it will take to completely transform the microstructure. In this study, the impingement is taken into account through the proper adjustment of the boundary conditions and interface locations. As shown in Fig. 6(a), when γ_1 dissolves first, δ_1 and δ_2 impinge on each other (hard impingement). It is assumed that the grain boundary between these two δ grains is stationary after impingement. Therefore, interfaces M1 and M2 vanish after the impingement, and no boundary condition is needed at the δ_1/δ_2 grain boundary. If γ_2 dissolves completely before γ_1, as indicated in Fig. 6(b), interface M3 is removed from the calculation domain. The boundary conditions for δ_2 are then adjusted as follows:
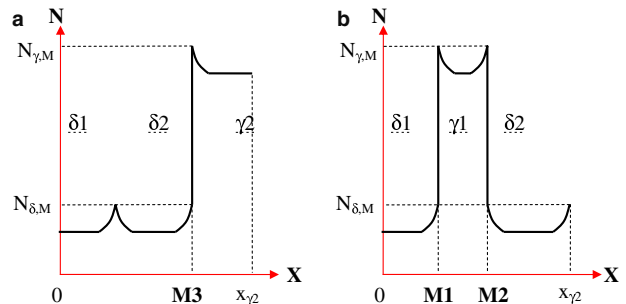

Fig. 6. Schematic plot showing the nitrogen concentration profile for the two circumstances at the moment when the smaller γ grain disappears: (a) γ_1 dissolves completely before γ_2, and (b) γ_2 dissolves completely before γ_1.

$$\delta_2: \quad N = N_{\delta,M} \quad \text{at } x = M2^+, \qquad \frac{\partial N}{\partial x} = 0 \quad \text{at } x = x_{\gamma_2}. \tag{11}$$

2.1.5. Thermodynamics of $\gamma \to \delta$ transformation

Hertzman et al. [5] evaluated the nitrogen concentrations in the δ and γ phases of a 2205 DSS under para-equilibrium conditions based on thermodynamic calculations. The calculated para-equilibrium concentration versus temperature data were then fitted to the form of $N = A + 10^{BT+C}$, where N is the concentration, A, B and C are coefficients, and T is the temperature. Based on their data, the para-equilibrium nitrogen concentrations are given as

$$N_{\delta,M} = 10^{0.002703 \times T - 5.04964} \quad (\text{wt.\%}), \tag{12}$$

$$N_{\gamma,M} = 0.255 + 10^{0.002257 \times T - 3.99984} \quad (\text{wt.\%}), \tag{13}$$

where $N_{\delta,M}$ is the nitrogen concentration in the δ phase, which is in para-equilibrium with γ, $N_{\gamma,M}$ is the nitrogen concentration in the γ phase, which is in para-equilibrium with δ, and T is temperature in Kelvin. The equilibrium fraction of γ (i.e., f_γ) can then be determined by using lever rule.

$$f_\gamma = \frac{N_C - N_{\delta,M}}{N_{\gamma,M} - N_{\delta,M}}, \tag{14}$$

where N_C is the nitrogen concentration in the base metal of the 2205 DSS.

The equilibrium fraction of γ has been experimentally measured in the literature [25] for a number of duplex stainless steels. The relationship of f_γ as a function of temperature and composition is given as [25]:

$$f_\gamma = 0.01[75 - 6.8 \times 10^{-15} \times T^5 + 190(C_C - 0.03)$$
$$+ 6(22 - Cr_C) + 9(Ni_C - 5) + 6.5(3 - Mo_C)$$
$$+ 160(N_C - 0.15)], \tag{15}$$

where C_C is the carbon concentration, Cr_C is the chromium concentration, Ni_C is the nickel concentration, Mo_C is the molybdenum concentration, and N_C is the nitrogen concentration. The concentrations of C, Cr, Ni, Mo and N in Eq. (15) are the average concentrations of elements in the base metal determined by chemical analysis. Substituting the composition of the 2205 DSS used in this study into Eq. (15), the f_γ versus temperature data are calculated, and these data are plotted in Fig. 7. Superimposed on these equilibrium calculations are the f_γ versus temperature data computed using Eqs. (12)–(14). As shown in Fig. 7, the correlation between the two curves is reasonable. Based on these para-equilibrium calculations, the completion temperature of the $\gamma \to \delta$ transformation, i.e., the temperature at which f_γ approaches zero, is 1592 K.

The start temperature of the $\gamma \to \delta$ transformation is assumed to be 1338 K. This temperature corresponds to
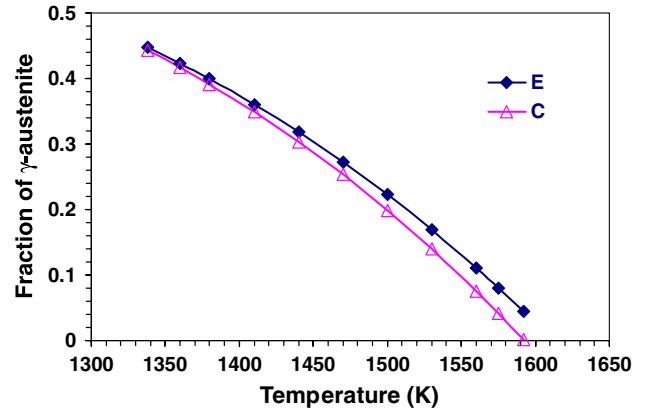

Fig. 7. The equilibrium fraction of γ as a function of temperature for the 2205 DSS. Curve E was obtained using the experimentally determined equation (Eq. (15)), whereas curve C was calculated using lever rule and the para-equilibrium nitrogen concentrations (Eqs. (12) and (13)).

the conditions used to prepare the final microstructure in the 2205 DSS base metal considered here. It should be noted that nitrogen can also diffuse at temperatures lower than 1338 K. In this study, the nitrogen diffusion below 1338 K was ignored, since no significant changes were observed in the base metal under the rapid weld heating conditions considered here [18,19]. Hence, 1338 K is only a nominal start temperature, and not the equilibrium temperature for the start of the $\gamma \to \delta$ transition.

2.1.6. Evaluating convergence of numerical solution

The convergence of the numerical calculations can be evaluated by checking the overall nitrogen mass conservation in the system. In the present study, the overall mass conservation is defined as

$$e_N = \frac{N_{cal} - N_{ini}}{N_{ini}} \times 100\%, \tag{16}$$

where e_N is an error representing the nitrogen mass conversation, N_{cal} is the calculated total mass of nitrogen at each time step, and N_{ini} is the initial mass of nitrogen in the system. An accurate solution requires that e_N approaches zero. At a given time step, the governing equations together with boundary conditions are solved iteratively until the error e_N is less than a predefined small number, say 1×10^{-4}. The calculation then advances one time step, and the solution at the new step is sought.

Different combinations of grid spacing and time step values were tested. The different grid spacing tested varied from 1 to 5×10^{-3} μm, whereas the time step tested differed from 10 to 0.02 ms. It was found that the value of e_N decreased to a low value, as the grid spacing and time step are reduced to a certain level. Further reduction of the grid spacing and time step did not change

the final results, while making the solution process much more computationally intensive. The optimal grid spacing and time step determined based on the tests are the following. The average initial grid spacing is around 5×10^{-2} μm, and spatially non-uniform grids were used to maximize the resolution of the calculations. Finer grid spacing was used in the vicinity of the δ/γ interface, since the nitrogen concentration gradient in this region is the highest. The time step used in the calculation was 0.1 ms. For the grid system and time step discussed above, the value of e_N was found to be fairly small, i.e., about 0.01%.

2.2. Weld heat transfer and fluid flow model

The thermo-fluid model used for the calculation of thermal cycles has been well tested in a number of different materials and welding systems [11,12, 26–30], and only salient features of the model are summarized here. The numerical model solves the equations of conservation of mass, momentum, and energy to obtain the velocity field in the weld pool and the temperature distribution over the entire weldment. The electromagnetic, surface tension gradient, and buoyancy forces, all of which drive the liquid metal convection in the weld pool, are taken into account. At the top surface of the weld, the heat loss due to the introduction of helium shielding gas is considered by using Newton's law of cooling with an appropriate heat transfer coefficient, as described in a previous paper [14]. Since the 2205 DSS contains 0.04 wt.% sulfur, the effect of sulfur on changing the surface tension was also included. The thermo-physical properties of the 2205 DSS [31] and other data used in the calculations are given in Table 2. The value of the arc efficiency was taken from a compilation of arc efficiency values available in [32]. In addition, this value re-

Table 2
Physical properties of the 2205 DSS and the other data used in the calculation [31]

Name	Value
Liquidus temperature (K)	1718.0
Solidus temperature (K)	1658.0
Density (kg m^{-3})	7200
Surface tension of liquid metal (N m^{-1})	Eq. (17)
Thermal conductivity of solid (J m^{-1} s^{-1} K^{-1})	20.0
Enhanced thermal conductivity of liquid (J m^{-1} s^{-1} K^{-1})	146.3
Enhanced viscosity of liquid metal (kg m^{-1} s^{-1})	0.08
Specific heat of solid (J kg^{-1} K^{-1})	560.1
Specific heat of liquid (J kg^{-1} K^{-1})	806.7
Magnetic permeability (N A^{-2})	1.26×10^{-6}
Coefficient of thermal expansion (K^{-1})	1.4×10^{-5}
Arc efficiency [32]	57.2%
Arc radius (mm)	2.8
Arc power distribution factor	0.5
Heat transfer coefficient at weld top surface (W m^{-2} K^{-1})	1.59×10^3

sulted in the calculation of correct weld pool shape and size and therefore is thought to be appropriate for the conditions of the experiments.

It should be noted that a rectangular solution domain was used to calculate the heat transfer and fluid flow in the cylindrical welding sample. Since the weld pool dimensions (10 mm wide and 4 mm deep) were much smaller than those of the cylindrical specimen (80 mm long and 102 mm diameter [18,19]), no significant error was introduced due to calculations in a flat geometry.

2.3. Experimental validation of nitrogen diffusion model

The SRXRD technique was used to obtain real-time kinetic data for the γ → δ transformation during welding. Several materials systems have been successfully studied using this technique, including commercially pure titanium [13], Ti–6Al–4V alloy [14], AISI 1005 plain carbon steel [15], AISI 1045 medium carbon steel [16], and AISI 304 austenitic stainless steel [17]. Prominent phase transformations specific to each alloy have been mapped, and significant insights into the associated kinetics of various phase transformations in the weld HAZ have been gained.

Gas tungsten arc (GTA) welds were made on 2205 DSS cylindrical bar samples. During welding, the surface of the 2205 DSS sample was irradiated with a high-intensity synchrotron beam, and the diffracted beam was collected to determine the crystal structure at discrete locations. The spatial distribution of the regions consisting of γ-austenite, δ-ferrite and liquid phases, and the boundaries between these regions were qualitatively identified. The diffraction data were further analyzed using a curve fitting routine to provide the relative fractions of γ and δ at locations across the width of the weld HAZ. Additional details of the SRXRD experiments are available elsewhere [18,19].

3. Results and discussion

3.1. Temperature and velocity fields in the weldment

The knowledge of temperature profiles in the weldment is a prerequisite for understanding the kinetics of phase transformations occurring during welding. The three-dimensional temperature and velocity fields were computed for the welding conditions considered here, and the results are shown in Fig. 8. In this figure, the temperatures are indicated by contour lines and the melt velocities are represented by arrows. Since the weld is symmetric about the $y = 0$ plane, only half of the weld is shown for clarity. As shown in Fig. 8, the convection pattern in the pool is complex due to the combined effect of surface tension gradient, electromagnetic and buoyancy forces. The 2205 DSS contains 0.004 wt.% of
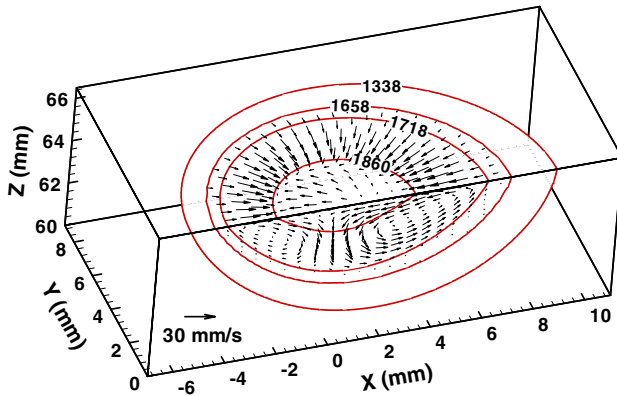
Fig. 8. Calculated temperature and velocity fields in three-dimension. All temperatures are given in Kelvin.

sulfur, which is enough to significantly affect the surface tension (γ) of the liquid metal. The effect of sulfur on the surface tension is calculated using the following equation for the Fe–S binary system [33].

$$\gamma = 1.943 - 4.3 \times 10^{-4}(T - 1809) - 1.3 \times 10^{-8}RT$$

$$\times \ln\left[1 + 0.00318a_S \exp\left(\frac{1.66 \times 10^5}{RT}\right)\right], \qquad (17)$$

where T is temperature in Kelvin, R is the universal gas constant (8.314 J mol^{-1}), and a_S is the activity of sulfur which is assumed to be equal to its concentration. Eq. (17) indicates the surface tension reaches a maximum value at 1860 K. In other words, the temperature coefficient of surface tension ($d\gamma/dT$) is greater than zero when the temperature is less than 1860 K, and vice versa. As a result, the liquid metal is pulled from the weld pool periphery to the 1860 K isotherm, whereas the melt flows outward in the center of the pool, as shown in Fig. 8. The downward flow in the middle of the pool is driven by the electromagnetic force.

Fig. 9 shows the comparison between the calculated and metallographically measured fusion zone (FZ) geometry. The calculated FZ boundary is represented by the 1658 K solidus isotherm. As shown in this figure, the calculated width and depth of the FZ agree
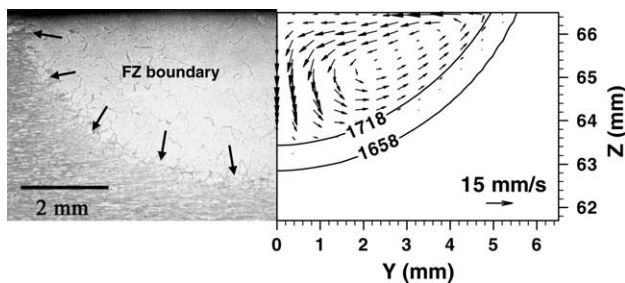
reasonably well with those measured experimentally. The good agreement at the FZ boundary means that the calculated HAZ temperatures should be equally accurate.

Fig. 10 shows the computed thermal cycles, which are calculated by converting the x distance into time using the welding speed, at various locations [30]. Due to the motion of the base metal relative to the heat source, the temperature field is slightly compressed in front of the heat source and elongated behind the heat source. As a result, the heating rates are higher than the cooling rates. As shown in Fig. 10, the peak temperatures and the heating and cooling rates decrease with increasing distance from the welding centerline, causing different phase transformations to take place at different locations across the weldment. For instance, at locations 1 through 3 in Fig. 10, the microstructural evolution sequence is expected to be the $\gamma \to \delta$ transformation, melting, solidification and $\delta \to \gamma$ transformation. At location 4, only $\gamma \to \delta$ transformation during heating and $\delta \to \gamma$ transformation during cooling may take place. Further away from the weld center, the temperatures are not high enough to initiate the $\gamma \to \delta$ transformation. The spatial variation of temperatures results in the spatial variation of microstructure in the weldment.

In some monitoring locations such as $Y = 3.5$ mm shown in Fig. 10, the peak temperature exceeded the liquidus temperature of the alloy and melting occurred. The final microstructure in these locations resulted from the cooling of the molten alloy and was different from that in the HAZ. However, it should be noted that all X-ray diffraction data used in the analysis were collected before the alloy melted and therefore pertinent for the understanding of $\gamma \to \delta$ transformation during heating of the solid.

Fig. 9. Comparison between experimental (left) and calculated (right) weld pool cross sections. Temperatures are given in Kelvin.
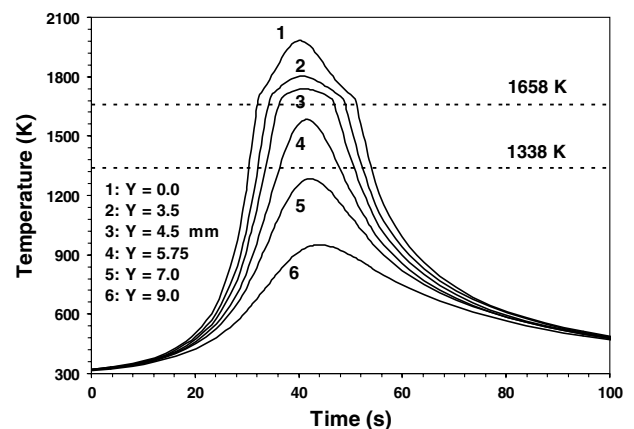

Fig. 10. Calculated thermal cycles at different locations. The Y location is defined as the distance to the weld centerline, as shown in Fig. 9. For the 2205 DSS, the solidus temperature is 1658 K and the starting temperature of the $\gamma \to \delta$ transformation is 1338 K. Locations 1, 2 and 3 are in the FZ while locations 4, 5 and 6 are in the HAZ.

3.2. Transformation kinetics for a system with uniform starting microstructure

Although the main focus of the present work is to understand the effects of a non-uniform starting structure, it is useful to first examine the transformation kinetics for a uniform starting structure. The domain with uniform structure shown in Fig. 2(a) was used in these calculations. Fig. 11 shows the calculated nitrogen concentration profile as a function of time at a monitoring location in the weld HAZ at $Y = 3.5$ mm. At this location, the peak temperatures experienced by the microstructure are high enough to drive the $\gamma \rightarrow \delta$ transformation to completion. At $t = 0$ s, the nitrogen concentration is uniformly distributed in each phase. As the temperature increases, the nitrogen concentration increases at each interface to a value higher than that in the bulk of each phase, and the interface moves into the higher nitrogen austenite phase. Towards the end of the transformation, the concentration gradients in both phases decrease as homogenization takes place.

Using the diffusion model and the corresponding thermal cycles, the kinetics of the $\gamma \rightarrow \delta$ transformation at two other locations in the weldment were calculated. The calculations were based on the uniform starting structure. Fig. 12 shows the comparison between the calculated and SRXRD experimentally determined transformation rates at these different locations. The agreement between the calculated and measured data seems reasonable, indicating the validity of the numerical diffusion model. Both the calculated and measured δ fraction versus time profiles resemble S-shape (sigmoidal) curves. Under the weld heating conditions experienced here, the transformation rate is initially slow, since both the temperature and diffusivity of nitrogen
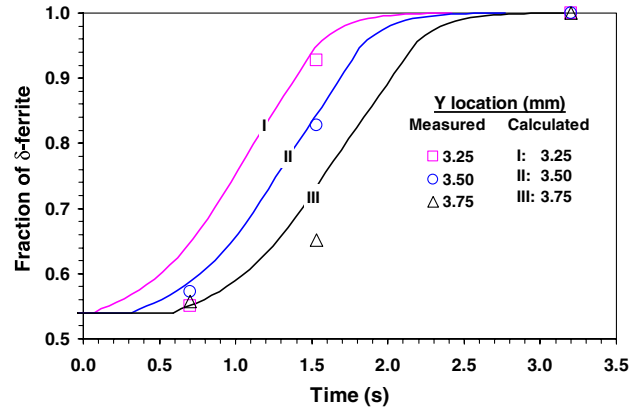
Fig. 12. Comparison of calculated and measured kinetic data at three different monitoring locations. Time zero is the same as that in Fig. 11. The uniform starting microstructure was used in the calculations.

are low at the beginning of the transformation. As the transformation proceeds, the temperature and the diffusivity of nitrogen, which depends exponentially on the temperature, increase, thus enhancing the transformation rate. Towards the end of the transformation, the increase in the nitrogen diffusivity no longer plays a dominant role, and the small concentration gradients and longer diffusion distances in the growing δ grain slow the transformation.

3.3. Effect of non-uniform starting microstructure

The effect of the non-uniform starting microstructure on the phase transformation rates was studied using the calculation domain consisting of two types of δ and γ grains with different sizes. Table 3 summarizes the five different starting microstructures. Case i has a uniform starting structure, and the average sizes for the γ and δ grains were used. Cases ii through v have non-uniform starting microstructures, with cases ii and iii having different γ grain sizes and cases iv and v having different δ grain sizes. For these cases, the sizes of the two grains comprising each phase are chosen so that their average is equal to that measured in the 2205 DSS base metal, as given by the following equation:

$$\frac{0.5W_{\delta_1} + W_{\delta_2}}{1.5} = \bar{W}_\delta = 22.3 \ \mu m$$

$$\frac{W_{\gamma_1} + 0.5W_{\gamma_2}}{1.5} = \bar{W}_\gamma = 19.0 \ \mu m$$

(18)

where $\bar{W}_\delta$ and $\bar{W}_\gamma$ are the average thicknesses of the δ and γ grains in the base metal, respectively. The coefficients of 0.5 and 1.5 are used to account for the actual number of grains in the calculation domain. As shown in Fig. 5, the total thickness of the δ grains is $(W_{\delta_1}/2) + W_{\delta_2}$, whereas the total number of δ grains is 3/2. Therefore, the mean thickness of δ grain in the system is $\frac{0.5W_{\delta_1} + W_{\delta_2}}{1.5}$. Similarly, the average γ grain thickness is
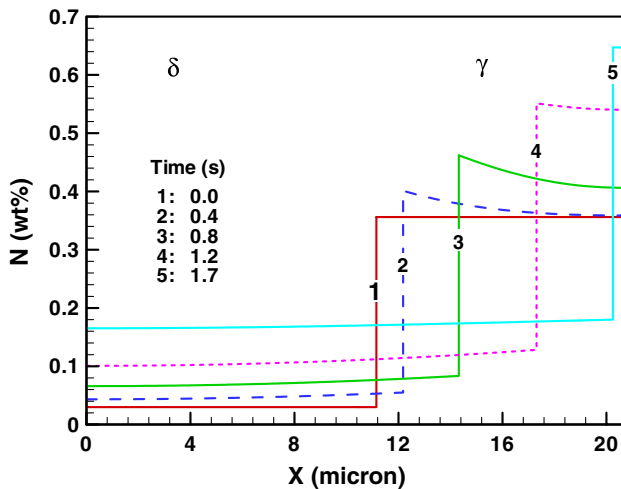
Fig. 11. Calculated nitrogen concentration profile as a function of time at $Y = 3.5$ mm location. The thermal cycle used is shown as the curve #2 in Fig. 10. Time zero corresponds to the moment when the 1338 K temperature is reached at this location.

Table 3
Summary of different starting microstructures used in the calculation of the $\gamma \to \delta$ transformation kinetics in the 2205 DSS

Case no.	$\frac{W_{\delta_1}}{2}$ (µm)	W_{γ_1} (µm)	W_{δ_2} (µm)	$\frac{W_{\gamma_2}}{2}$ (µm)	Amount of δ (µm)	Amount of γ (µm)	δ/γ phase ratio
i	11.15	19.0	22.3	9.5	33.45	28.5	1.17
ii	11.15	5.0	22.3	23.5	33.45	28.5	1.17
iii	11.15	23.5	22.3	5.0	33.45	28.5	1.17
iv	5.15	19.0	28.3	9.5	33.45	28.5	1.17
v	28.3	19.0	5.15	9.5	33.45	28.5	1.17

Thicknesses W_{δ_1}, W_{δ_2}, W_{γ_1}, and W_{γ_1} are defined in Fig. 5. Case i has a uniform starting structure, whereas cases ii through v have starting structures with varying degrees of non-uniformity.

$\frac{W_{\gamma_1} + 0.5W_{\gamma_2}}{1.5}$. As shown in Table 3, for all the five starting structures, the amounts of the δ and γ grains in the calculation domain are 33.45 and 28.5 µm, respectively, yielding a δ/γ phase ratio of 1.17.

Fig. 13 shows the calculated nitrogen concentration profile versus time for case ii at $Y = 3.5$ mm. The structure in this case consists of a very small γ grain (5.0 µm) and a fairly large γ grain (47.0 µm). For this starting microstructure, the γ_1 grain dissolves completely at a time of approximately 0.9 s and a temperature of 1486 K. As a result, the δ_1 and δ_2 grains impinge, and interfaces M1 and M2 disappear. After the dissolution of the γ_1 grain, the transformation is controlled only by the movement of the interface M3.

The calculated nitrogen concentration profile versus time for case iii, where γ_2 has a smaller thickness than γ_1, is shown in Fig. 14. The γ grain thicknesses for case iii lie in between those for cases i and ii: the large γ grain has a thickness of 23.5 µm and the small one has a thickness of 10.0 µm. As shown in this figure, the γ_2 grain dissolves completely before γ_1, and the interface M3 vanishes. Both interface M1 and M2 continue to move

Fig. 14. Calculated nitrogen concentration profile as a function of time for case iii starting microstructure in Table 3.

until the γ_1 grain dissolves completely. Both Figs. 13 and 14 indicate that at the end of transformation, the nitrogen diffusion in the larger γ grain controls the overall transformation rate.

Fig. 15 summarizes the phase transformation rates for these five starting microstructures at the $Y = 3.5$ mm location. As shown in this figure, the transformation rates are fastest for the uniform structure in case i. Non-uniform starting structures display slower transformation kinetics, particularly toward the end of the transformation. Fig. 15 shows that for case i, the $\gamma \to \delta$ transformation reaches completion at a time of $t = 2.4$ s. For the four non-uniform structures, the transformation completes at least 0.7 s later. In other words, the transformation takes 30% more time to complete for the non-uniform structures than the uniform one. It is also shown that large deviations from the average γ size slow the transformation rate, since the small γ grain dissolves completely at first, and the transformation kinetics are then controlled by the nitrogen diffusion in the large γ grain.

It is also interesting to note that the existence of a small γ grain does not speed up the transformation rate at the beginning of the reaction. The interface moving
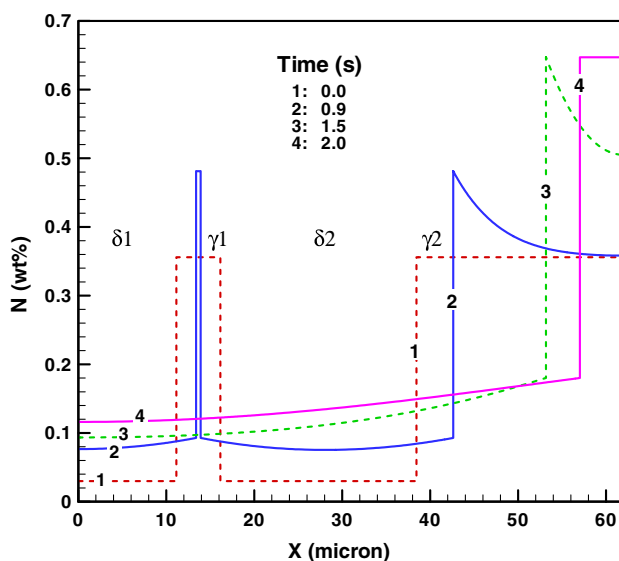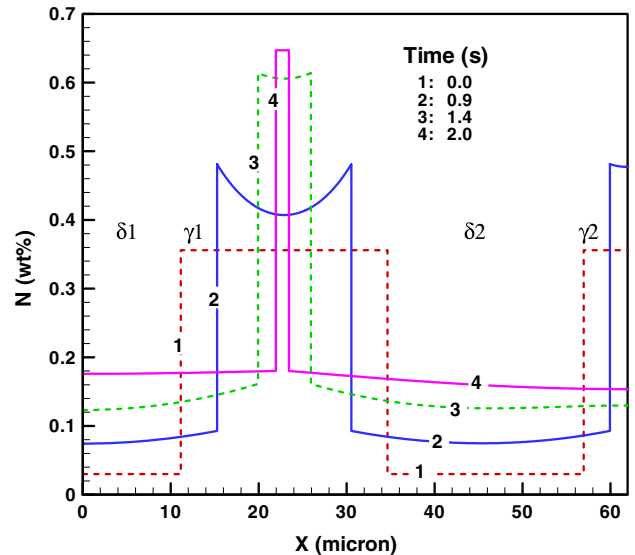

Fig. 13. Calculated nitrogen concentration profile as a function of time for case ii starting microstructure in Table 3. The thermal cycle at $Y = 3.5$ mm was used in the calculation.
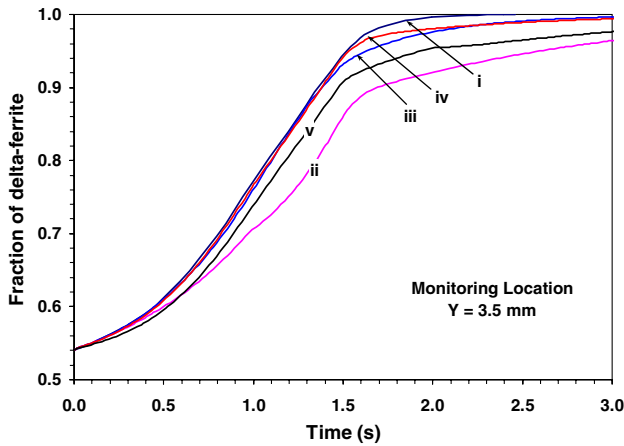
Fig. 15. Ferrite fraction versus time plot for the five cases of starting microstructures shown in Table 3. Case i represents the uniform starting structure while cases ii through v correspond to non-uniform starting structures.

velocity, which determines the overall transformation kinetics, depends mostly on the rate at which the nitrogen diffuses away from the δ/γ interface into the γ and δ grains, as indicated by Eq. (6). Since the γ grain size does not significantly affect the interface moving velocity, the transformation rates for cases i through iii are similar at the beginning of the reaction. However, toward the end of the transformation, the small γ grain completely dissolves before the large one. As a result, only one δ/γ interface is still moving, and the other two interfaces impinge on each other, as illustrated in Fig. 13. Therefore, the overall transformation rates slow considerably.

The effect of the non-uniformity in the δ grain size on the transformation kinetics is shown in cases iv and v in Fig. 15. It is found that the larger the deviation from the average δ thickness, the slower the transformation rate. However, it seems that the variation in the δ grain thicknesses has a less significant effect on the transformation rates than changes in the γ grain thicknesses. This behavior is expected because of the role played by the δ/γ interfacial area. For cases i, iv and v, the two γ grains in the system have the same thickness, and they completely dissolve only at the end of the transformation. Three moving δ/γ interfaces exist in the system throughout the majority of the transformation. Therefore, the interfacial area, in which the γ phase is in contact with the δ phase, has not been changed, even though the δ grains are made larger. As a result, the transformation rates are not significantly affected by the δ grain sizes.

Note that the assumptions made in this model may limit its applications to other alloy systems similar to the DSS alloy studied here. First, constant interfacial area was considered in the model. In some alloys, the non-uniformity in the microstructure may also result in transformation rates that are different from those

computed here. Second, the system used here has a one-dimensional geometry, which provides a reasonable approximation of the microstructure in the 2205 DSS. The microstructure in many real materials has a three-dimensional shape, and this factor has not been investigated here. However, a recent study [34] based on the Avrami theory, considering the nucleation and growth in three dimensions, suggested similar trends as those predicted using the one-dimensional diffusion model. It was also found [34] that the initial transformation rate was not significantly affected by the non-uniform structure, whereas the completion of the transformation was significantly delayed. Finally, the system used here consists of four grains. A more comprehensive study taking into account more complex structure is left for future efforts.

3.4. TTT and CHT diagrams

There are two main types of transformation diagrams that provide useful graphical representation of the transformation kinetics: TTT and CHT diagrams. The former predicts isothermal transformation kinetics, whereas the latter considers transformation kinetics during heating. After the numerical diffusion model was validated, TTT and CHT diagrams were developed for the $\gamma \to \delta$ transformation in the 2205 DSS.

For the TTT diagram, various constant temperatures above 1338 K, i.e., the nominal start temperature of the transformation, were used. At each temperature, the δ fraction as a function of time was calculated, and the results were used to construct a TTT diagram, which is shown in Fig. 16. The 55% and 99% curves are assumed to represent the start and completion of the $\gamma \to \delta$ transformation. As shown in this figure, the rates of the γ
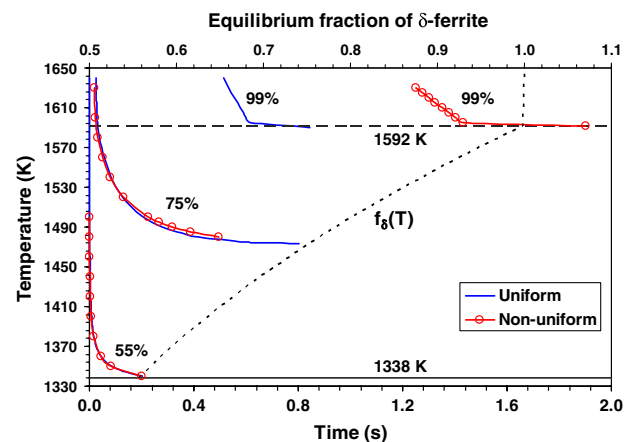

Fig. 16. Calculated TTT diagram for the $\gamma \to \delta$ transformation during heating of the 2205 DSS. The 1338 and 1592 K are the nominal start and completion temperatures of the transformation, respectively. Superimposed are the para-equilibrium fraction of δ phase versus temperature data ($f_\delta(T)$) calculated based on Eqs. (12) and (13).

dissolution accelerate rapidly as the temperature and diffusivity of nitrogen in γ and δ increase. In addition, the interface concentration of nitrogen increases with temperature, and the driving force for diffusion is consequently increased. The effect of the non-uniform starting structure on the isothermal transformation kinetics is also illustrated in this figure. The uniform and non-uniform microstructures correspond to cases i and iii in Table 3, respectively. As shown in this figure, the 55% and 75% δ profiles are unaffected by the starting microstructure, whereas the 99% profile for the non-uniform structure is delayed compared to that for the uniform structure.

It should be noted that in the TTT diagram, the maximum δ fraction converted at a given temperature is equal to the equilibrium δ fraction at that temperature, as indicated by the dashed line in this figure. For example, an equilibrium fraction of 0.75 is reached only when the temperature rises above 1474 K. As a result, the two 75% curves are leveling off at this temperature. In other words, the calculated TTT diagram indicates that the δ fraction cannot be higher than 75% at temperatures lower than 1474 K, which is consistent with the phase equilibria of the 2205 DSS.

In the CHT diagram, the time–temperature relationship is expressed as: $T(t) = 1338 + H_T \times t$, where H_T is the heating rate (K s^{-1}), and t is the time. The non-isothermal transformation kinetics at various heating rates were calculated using the numerical diffusion model, and the resulting δ fraction versus time data were then used to construct the CHT diagram. Fig. 17 shows the computed CHT diagram for the $\gamma \rightarrow \delta$ transformation, where time zero represents the moment when the 1338 K temperature is reached. Superimposed in this figure are the SRXRD experimental data points, at which the completion of the $\gamma \rightarrow \delta$ transformation is observed. These data points were plotted using the average heating rates at respective monitoring locations during this

transformation. The SRXRD data points scattered in the area where the heating rates vary from 75 to 200 K s^{-1}. Similar to those shown in the TTT diagram, the 55% and 75% δ profiles are unaffected by the starting structure. On the other hand, the non-uniform structure significantly delays the completion of the transformation. The SRXRD experimental data lie in between the two 99% profiles for the uniform and non-uniform structures. A comparison between Figs. 16 and 17 indicates the non-uniform starting microstructure delays the completion of the $\gamma \rightarrow \delta$ transformation under both iso-thermal and non-isothermal conditions.

4. Summary and conclusions

Kinetics of the $\gamma \rightarrow \delta$ transformation during GTA welding of 2205 DSS was simulated using a combination of thermo-fluid and diffusion models considering non-uniform initial microstructure. These results were then validated using experimental data obtained using a SRXRD technique. The following conclusions can be made from the present investigation.

(1) The thermal cycles needed for the phase transformation model were computed using a well tested three-dimensional heat transfer and fluid flow model. Since the presence of sulfur in the base metal affects the nature of the metal flow in the weld pool and the convective heat transfer, the presence of sulfur in the 2205 DSS steel was taken into account in calculating the thermal cycles. The reliability of the calculated temperature field was confirmed by the agreement between the computed and the experimental FZ geometry.

(2) A numerical diffusion model using a moving grid system to trace the moving interfaces was developed to calculate the kinetics of $\gamma \rightarrow \delta$ transformation during heating of the 2205 DSS. The predicted transformation kinetics agreed reasonably well with those measured using the SRXRD technique at various monitoring locations in the weldment. The calculated fraction converted curve exhibits an S-shaped profile as a result of the non-isothermal heating.

(3) The effect of non-uniform starting microstructures on the transformation rate was studied considering a system with two types of γ grains and δ grains of distinct sizes. It is found that the overall transformation rate is fastest when the starting structure is uniform. A non-uniform starting structure slows the transformation rate, particularly toward the end of the transformation. For the four non-uniform structures considered here, the transformation takes at least 30% more time to complete than for the uniform structure. This decrease in the transformation rate results from the reduction of the δ/γ interface area caused by the dissolution of the small γ grains at an early stage of the transformation. The overall reaction rate is then controlled by the nitrogen
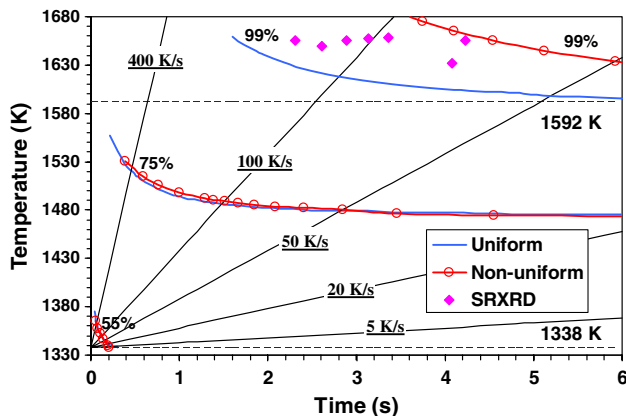

Fig. 17. Calculated CHT diagram for the $\gamma \rightarrow \delta$ transformation during heating of the 2205 DSS. Solid diamonds represent the experimental data points at which the completion of the transformation is observed.

diffusion in large γ grains. The variation of γ grain size has a more significant effect on retarding the transformation kinetics than that of δ grain size.

(4) TTT and CHT diagrams were calculated for the 2205 DSS using the numerical diffusion model, providing a graphical means to predict the kinetics of the $\gamma \rightarrow \delta$ transformation. Both TTT and CHT diagrams show that the transformation rate increases with temperature and the non-uniform starting structure delays the completion of the transformation. The calculated results agreed fairly well with the data measured using the SRXRD technique.

Acknowledgements

References

[1] Metals Handbook: Properties and Selection: Iron, Steels, and High Performance Alloys, 10th edn, vol. 1, ASM International, Materials Park, OH, 1990.
[2] Gunn RN. Duplex stainless steels: microstructure, properties and applications. Cambridge: Abington Publishing; 1997.
[3] Hemmer H, Grong Ø. Metall. Mater. Trans. A 1999;30:2915.
[4] Hemmer H, Klokkehaug S, Grong Ø. Metall. Mater. Trans. A 2000;31:1035.
[5] Hertzman S, Ferreira PJ, Brolund B. Metall. Mater. Trans. A 1997;28:277.
[6] Engberg G, Hillert M, Odén A. Scand. J. Metall. 1975;4:93.
[7] Akbay T, Reed RC, Atkinson C. Acta Metall. Mater. 1994;47:1469.
[8] Atkinson C, Akbay T, Reed RC. Acta Metall. Mater. 1995;43:2013.
[9] Mancini R, Budde C. Acta Mater. 1999;47:2907.
[10] Yang JR, Bhadeshia HKDH. Mater. Sci. Eng. A 1991;131:99.
[11] Mundra K, DebRoy T, Kelkar KM. Numer. Heat Transfer A 1996;29:115.
[12] Zhang W, Roy GG, Elmer JW, DebRoy T. J. Appl. Phys. 2003;93:3022.
[13] Yang Z, Elmer JW, Wong J, DebRoy T. Weld. J. 2000;79:97s.
[14] Elmer JW, Palmer TA, Babu SS, Zhang W, DebRoy T. J. Appl. Phys. 2004;95:8327.
[15] Elmer JW, Palmer TA, Zhang W, Wood B, DebRoy T. Acta Mater. 2003;51:3333.
[16] Elmer JW, Palmer TA, Babu SS, Zhang W, DebRoy T. Weld. J. 2004;83:244s.
[17] Elmer JW, Wong J, Ressler T. Scripta Mater. 2000;43:751.
[18] Palmer TA, Elmer JW, Wong J. Sci. Technol. Weld. Joining 2002;7:159.
[19] Palmer TA, Elmer JW, Babu SS. Mater. Sci. Eng. A 2004;374:307.
[20] Shewmon P. Diffusion in solids. 2nd ed. Warrendale (PA): TMS; 1989.
[21] Rhee B, Roh S, Kim D. Materials transactions. The Japan Institute of Metals 2003;44:1014.
[22] Murray WD, Landis F. Journal of heat transfer. Trans ASME 1959;81:106.
[23] Crank J. The mathematics of diffusion. 2nd ed. Oxford: Clarendon Press; 1975.
[24] Patankar SV. Numerical heat transfer and fluid flow. New York (NY): McGraw-Hill; 1980.
[25] Hertzman S, Roberts W, Lindenmo M. In: Proceedings of Duplex Stainless Steels 86, The Hague, The Netherlands; 1986. p. 257.
[26] Mishra S, DebRoy T. Acta Mater. 2004;52:1183.
[27] He X, Fuerschbach P, DebRoy T. J. Appl. Phys. 2004;96:4547.
[28] Kumar A, Mishra S, Elmer JW, DebRoy T. Metal Mater Trans A 2005;36A:15.
[29] Zhang W, Kim C-H, DebRoy T. J. Appl. Phys. 2004;95:5210.
[30] Zhang W, Kim C-H, DebRoy T. J. Appl. Phys. 2004;95:5220.
[31] Cverna F. Thermal properties of metals. Materials Park (OH): ASM International; 2002.
[32] Kou. Welding metallurgy. New York (NY): John Wiley and Sons; 1987.
[33] Sahoo P, DebRoy T, McNallan MJ. Metall Trans B 1988;19:483.
[34] Matsuda H, Bhadeshia HKDH. Mater Sci Technol 2003;19:1330.